

Ab initio phonon coupling and optical response of hot electrons in plasmonic metals

Ana M. Brown,¹ Ravishankar Sundararaman,² Prineha Narang,^{1,2,3} William A. Goddard III,^{2,4} and Harry A. Atwater^{1,2}

¹Thomas J. Watson Laboratories of Applied Physics, California Institute of Technology, Pasadena CA

²Joint Center for Artificial Photosynthesis, California Institute of Technology, Pasadena CA

³NG NEXT, 1 Space Park Drive, Redondo Beach CA

⁴Materials and Process Simulation Center, California Institute of Technology, Pasadena CA

(Dated: March 19, 2024)

Ultrafast laser measurements probe the non-equilibrium dynamics of excited electrons in metals with increasing temporal resolution. Electronic structure calculations can provide a detailed microscopic understanding of hot electron dynamics, but a parameter-free description of pump-probe measurements has not yet been possible, despite intensive research, because of the phenomenological treatment of electron-phonon interactions. We present *ab initio* predictions of the electron-temperature dependent heat capacities and electron-phonon coupling coefficients of plasmonic metals. We find substantial differences from free-electron and semi-empirical estimates, especially in noble metals above transient electron temperatures of 2000 K, because of the previously-neglected strong dependence of electron-phonon matrix elements on electron energy. We also present first-principles calculations of the electron-temperature dependent dielectric response of hot electrons in plasmonic metals, including direct interband and phonon-assisted intraband transitions, facilitating complete *ab initio* predictions of the time-resolved optical probe signatures in ultrafast laser experiments.

I. INTRODUCTION

Understanding the energy transfer mechanisms during thermal non-equilibrium between electrons and the lattice is critical for a wide array of applications. Non-equilibrium electron properties on time scales of 10-100s of femtoseconds are most efficiently observed with pulsed laser measurement techniques.¹⁻⁷ Laser irradiation of a metal film or nanostructure with an ultrashort laser pulse pushes the electron gas out of equilibrium; describing the evolution of this non-equilibrium distribution has been the subject of intense research for two decades.⁸⁻¹² A majority of investigations so far employ various approximate models, typically based on free-electron models and empirical electron-phonon interactions, to calculate the energy absorption, electron-electron thermalization and electron-phonon relaxation.¹³⁻¹⁸ However, a complete *ab initio* description of the time evolution and optical response of this non-equilibrium electron gas from femtosecond to picosecond time scales has remained elusive, especially because of the empirical treatment of electron-phonon interactions.¹⁹

The initial electron thermalization via electron-electron scattering is qualitatively described within the Landau theory of Fermi liquids.²⁰⁻²³ The subsequent relaxation of the high temperature electron gas with the lattice is widely described by the two-temperature model (TTM),^{5-7,17,19} given by coupled differential equations for the electron and lattice temperatures, T_e and T_l ,

$$\begin{aligned} C_e(T_e) \frac{dT_e}{dt} &= \nabla \cdot (\kappa_e \nabla T_e) - G(T_e) \times (T_e - T_l) + S(t) \\ C_l(T_l) \frac{dT_l}{dt} &= \nabla \cdot (\kappa_p \nabla T_p) + G(T_e) \times (T_e - T_l). \end{aligned} \quad (1)$$

Here, κ_e and κ_p are the thermal conductivities of the electrons and phonons, $G(T_e)$ is the electron-phonon coupling factor, $C_e(T_e)$ and $C_l(T_l)$ are the electronic and lattice

heat capacities, and $S(t)$ is the source term which describes energy deposition by a laser pulse. In nanostructures, the temperatures become homogeneous in space rapidly and the contributions of the thermal conductivities drop out. A vast majority of studies treat the remaining material parameters, $G(T_e)$, $C_e(T_e)$ and $C_l(T_l)$, as phenomenological temperature-independent constants.

A key challenge in the quantitative application of TTM models is the determination of these *temperature-dependent* material parameters. With pulsed lasers, it is possible to absorb sufficient energy in plasmonic nanostructures to melt the metal once the electrons and lattice have equilibrated.²⁴ The highest electron temperature, T_e^{\max} accessible in repeatable measurements is therefore limited only by the equilibrated lattice temperature being less than the melting temperature T_m of the metal,²⁵ which yields the condition $\int_{T_m}^{T_e^{\max}} dT_e C_e(T_e) = \int_{T_0}^{T_m} dT_l C_l(T_l)$. Starting at room temperature $T_0 = 300$ K and using our *ab initio* calculations of the electron and lattice heat capacities, $C_e(T_e)$ and $C_l(T_l)$, we find $T_e^{\max} \approx 5700, 8300, 7500$ and 6700 K respectively for aluminum, silver, gold and copper. For gold and copper in particular, these temperatures are sufficient to change the occupations of the d -bands ~ 2 eV below the Fermi level. Consequently, it is important to derive the temperature dependence of these material parameters from electronic structure calculations rather than free-electron like models.¹⁹

To accurately predict the transient optical response of metal nanostructures, we account for the electron-temperature dependence of the electronic heat capacity, electron-phonon coupling factor and dielectric functions. These properties, in turn, require accurate electron and phonon band structures as well as electron-phonon and optical matrix elements. We recently showed that *ab initio* calculations can quantitatively predict optical response, carrier generation and electron transport in plas-

monic metals in comparison with experiment, with no empirical parameters.²⁶ In this article, we calculate $C_e(T_e)$, $G(T_e)$ and the temperature and frequency-dependent dielectric function, $\epsilon(\omega, T_e)$ from first principles. These calculations implicitly include electronic-structure effects in the density of states and electron-phonon interaction matrix elements, and implicitly account for processes such as Umklapp scattering. We show substantial differences between our fully *ab initio* predictions and those from simplified models due to the energy dependence of the electron-phonon matrix elements, especially at high electron temperatures.

The paper is organized as follows. We start with the theoretical background and computational methods used in the calculations of the electron heat capacity, *ab initio* phonon coupling and temperature dependent *ab initio* dielectric function of plasmonic materials (Section II A). In Section IIB, we show calculations of the electron heat capacity and its dependence on the electron temperature due to the electronic density of states. Analogously, section IIC presents the lattice-temperature dependence of the lattice heat capacity due to the phonon density of states. Next, in Section IID we show a key result of the paper: temperature dependence of the electron-phonon coupling strength accounting for energy dependence of the electron-phonon matrix elements. Finally, section IIE presents the temperature and frequency dependence of the *ab initio* dielectric function, including direct (inter-band), phonon-assisted and Drude intraband contributions. Section III summarizes our results and discusses their application to plasmonic nanostructures in various experimental regimes.

II. THEORY AND RESULTS

A. Computational details

We perform *ab initio* calculations of the electronic states, phonons, electron-phonon and optical matrix elements, and several derived quantities based on these properties, for four plasmonic metals, aluminum, copper, silver and gold. We use the open-source JDFTx plane-wave density functional software²⁷ to perform fully relativistic (spinorial) band structure calculations using norm-conserving pseudopotentials at a kinetic energy cut-off of 30 Hartrees, and the PBEsol exchange-correlation functional²⁸ with a localized ‘+*U*’ correction²⁹ for the *d*-bands in the noble metals. Ref. 30 shows that this method produces accurate electronic band structures in agreement with angle-resolved photoemission (ARPES) measurements within 0.1 eV.

We calculate phonon energies and electron-phonon matrix elements using perturbations on a $4 \times 4 \times 4$ supercell. In *ab initio* calculations, these matrix elements implicitly include Umklapp-like processes. We then convert the electron and phonon Hamiltonians to a maximally-localized Wannier function basis,³¹ with 12^3 *k*-points in the Brillouin zone for electrons. Specifically, we employ 24 Wannier centers for aluminum and 46 spinorial cen-

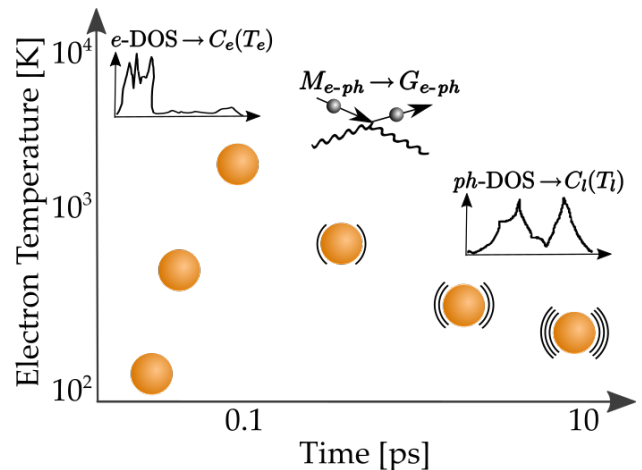


FIG. 1. Figure 1 represents the evolution of the non-equilibrium ‘hot’ electrons with time with different regimes dominated by distinct material properties. The electronic density of states (DOS) determines the electronic heat capacity $C_e(T_e)$ and the temperature to which the electrons equilibrate. The electron-phonon coupling $G(T_e)$ determines the dynamics of energy transfer from the electrons to the phonons. The phonon DOS determines the lattice heat capacity C_l and the temperature to which the lattice equilibrates. All of these properties are particularly sensitive to the electron temperature T_e , and are essential for a quantitative description of the ultrafast response of plasmonic metals under laser excitation.

ters for the noble metals which reproduces the DFT band structure exactly to at least 50 eV above the Fermi level.

Using this Wannier representation, we interpolate the electron, phonon and electron-phonon interaction Hamiltonians to arbitrary wave-vectors and perform dense Monte Carlo sampling for accurately evaluating the Brillouin zone integrals for each derived property below. This dense Brillouin zone sampling is necessary because of the large disparity in the energy scales of electrons and phonons, and directly calculating DFT phonon properties on dense *k*-point grids is computationally expensive and impractical. See Ref. 26 for further details on the *ab initio* calculation protocol and benchmarks of the accuracy of the electron-phonon coupling (eg. resistivity within 5% for all four metals).

B. Electronic density of states and heat capacity

The electronic density of states (DOS) per unit volume

$$g(\epsilon) = \int_{\text{BZ}} \frac{d\mathbf{k}}{(2\pi)^3} \sum_n \delta(\epsilon - \epsilon_{\mathbf{k}n}), \quad (2)$$

where $\epsilon_{\mathbf{k}n}$ are energies of quasiparticles with band index *n* and wave-vector **k** in the Brillouin zone BZ, directly determines the electronic heat capacity and is an important factor in the electron-phonon coupling and dielectric response of hot electrons. Above, the band index *n* implicitly counts spinorial orbitals in our relativistic calcu-

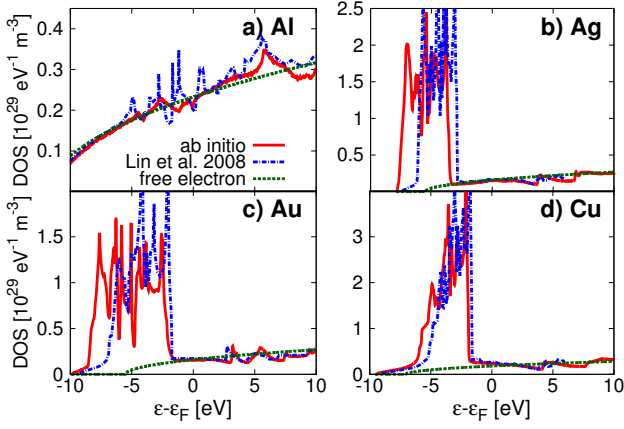


FIG. 2. Comparison of electronic density of states of for (a) Al, (b) Ag, (c) Au and (d) Cu from our relativistic PBEsol+ U calculations (*ab initio*), previous semi-local PBE DFT calculations¹⁹ (less accurate band structure), and a free electron model.

lations, and hence we omit the explicit spin degeneracy factor.

Figure 2 compares the DOS predicted by our relativistic PBEsol+ U method with a previous non-relativistic semi-local estimate¹⁹ using the PBE functional,³² as well as a free electron model $\varepsilon_{\mathbf{k}} = \frac{\hbar^2 k^2}{2m_e}$ for which $g(\varepsilon) = \frac{\sqrt{\varepsilon}}{2\pi^2} \left(\frac{2m_e}{\hbar^2}\right)^{3/2}$. The free electron model is a reasonable approximation for aluminum and the PBE and PBEsol+ U density-functional calculations also agree reasonably well in this case. The regular 31^3 k -point grid used for Brillouin zone sampling introduces the sharp artifacts in the DOS from Ref. 19, compared to the much denser Monte Carlo sampling in our calculations with 640,000 k -points for Au, Ag, and Cu, and 1,280,000 k -points for Al.

For the noble metals, the free electron model and the density functional methods agree reasonably near the Fermi level, but differ significantly ~ 2 eV below the Fermi level where d -bands contribute. The free electron models ignore the d -bands entirely, whereas the semi-local PBE calculations predict d -bands that are narrower and closer to the Fermi level than the PBEsol+ U predictions. The U correction²⁹ accounts for self-interaction errors in semi-local DFT and positions the d -bands in agreement with ARPES measurements (to within ~ 0.1 eV).³⁰ Additionally, the DOS in the non-relativistic PBE calculations strongly peaks at the top of the d -bands (closest to the Fermi level), whereas the DOS in our relativistic calculations is comparatively balanced between the top and middle of the d -bands due to strong spin-orbit splitting, particularly for gold. Below, we find that these inaccuracies in the DOS due to electronic structure methods previously employed for studying hot electrons propagates to the predicted electronic heat capacity and electron-phonon coupling.

The electronic heat capacity, defined as the derivative of the electronic energy per unit volume with respect to the electronic temperature (T_e), can be related to the

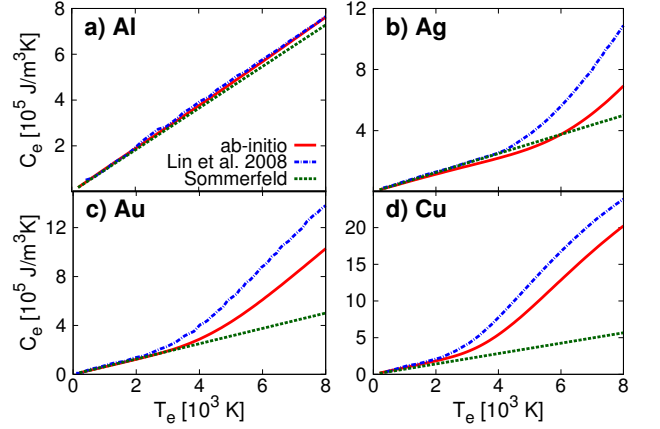


FIG. 3. Comparison of the electronic heat capacity as a function of electron temperature, $C_e(T_e)$, for (a) Al, (b) Ag, (c) Au and (d) Cu, corresponding to the three electronic density-of-states predictions shown in Figure 2. The free electron Sommerfeld model underestimates C_e for noble metals at high T_e because it neglects d -band contributions, whereas previous DFT calculations¹⁹ overestimate it because their d -bands are too close to the Fermi level.

DOS as

$$C_e(T_e) = \int_{-\infty}^{\infty} d\varepsilon g(\varepsilon) \varepsilon \frac{\partial f(\varepsilon, T_e)}{\partial T_e}, \quad (3)$$

where $f(\varepsilon, T_e)$ is the Fermi distribution function. The term $\partial f / \partial T_e$ is sharply peaked at the Fermi energy ε_F with a width $\sim k_B T_e$, and therefore the heat capacity depends only on electronic states within a few $k_B T_e$ of the Fermi level. For the free electron model, Taylor expanding $g(\varepsilon)$ around ε_F and analytically integrating (3) yields the Sommerfeld model $C_e(T_e) = \frac{\pi^2 n_e k_B^2}{2\varepsilon_F} T_e$, which is valid for $T_e \ll T_F$ ($\sim 10^5$ K). Above, $n_e = 3\pi^2 k_F^3$, $\varepsilon_F = \frac{\hbar^2 k_F^2}{2m_e}$ and k_F are respectively the number density, Fermi energy and Fermi wave-vector of the free electron model.

At temperatures $T_e \ll T_F$, the electronic heat capacities are much smaller than the lattice heat capacities,^{5,10,22} which makes it possible for laser pulses to increase T_e by $10^3 - 10^4$ Kelvin, while T_l remains relatively constant.^{6,33,34} Figure 3 compares $C_e(T_e)$ from the free-electron Sommerfeld model with predictions of (3) using DOS from PBE and PBEsol+ U calculations. The free-electron Sommerfeld model is accurate at low temperatures (up to ~ 2000 K) for all four metals.

With increasing T_e , $\partial f / \partial T_e$ in (3) is non-zero increasingly further away from the Fermi energy, so that deviations from the free electron DOS eventually become important. For aluminum, the DOS remains free-electron-like over a wide energy range and the Sommerfeld model remains valid throughout. For the noble metals, the increase in DOS due to d -bands causes a dramatic increase in $C_e(T_e)$ once T_e is high enough that $\partial f / \partial T_e$ becomes non-zero in that energy range. Copper and gold have shallower d -bands and deviate at lower temperatures compared to silver. Additionally, the d -bands are too close to the Fermi level in the semilocal PBE calculations

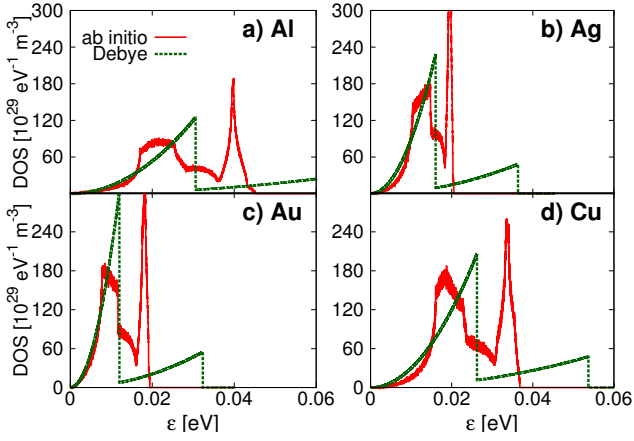


FIG. 4. Comparison of *ab initio* phonon density of states and the Debye model for (a) Al, (b) Ag, (c) Au and (d) Cu.

of Ref. 19 which results in an overestimation of $C_e(T_e)$ compared to our predictions based on the more accurate relativistic PBEsol+ U method.

C. Phonon density of states and lattice heat capacity

Similarly, the phonon DOS per unit volume

$$D(\varepsilon) = \int_{\text{BZ}} \frac{d\mathbf{q}}{(2\pi)^3} \sum_{\alpha} \delta(\varepsilon - \hbar\omega_{\mathbf{q}\alpha}), \quad (4)$$

where $\hbar\omega_{\mathbf{q}\alpha}$ are energies of phonons with polarization index α and wave-vector \mathbf{q} , directly determines the lattice heat capacity,

$$C_l(T_l) = \int_0^\infty d\varepsilon D(\varepsilon) \varepsilon \frac{\partial n(\varepsilon, T_l)}{\partial T_l}, \quad (5)$$

where $n(\varepsilon, T_l)$ is the Bose occupation factor.

Within the Debye model, the phonon energies are approximated by an isotropic linear dispersion relation $\omega_{\mathbf{q}\alpha} = v_{\alpha}q$ up to a maximum Debye wave vector q_D chosen to conserve the number of phonon modes per unit volume. This model yields the analytical phonon DOS, $D(\varepsilon) = \frac{\varepsilon^2}{(2\pi^2)} \sum_{\alpha} \theta(\hbar q_D v_{\alpha} - \varepsilon) / (\hbar v_{\alpha})^3$, where $v_{\alpha} = \{v_L, v_T, v_T\}$ are the speeds of sound for the one longitudinal and two degenerate transverse phonon modes of the face-centered cubic metals considered here.²⁵

Figure 4 compares the *ab initio* phonon DOS with the Debye model predictions, and shows that the Debye model is a good approximation for the DOS only up to 0.01 eV. However, Figure 5 shows that the corresponding predictions for the lattice heat capacities are very similar, rapidly approaching the equipartition theorem prediction of $C_l = 3k_B/\Omega$ at high temperatures, which is insensitive to details in the phonon DOS. In fact, the largest deviations of the Debye model are below 100 K and less than 10 % from the *ab initio* predictions for all four metals. We therefore find that a simple model of the phonons

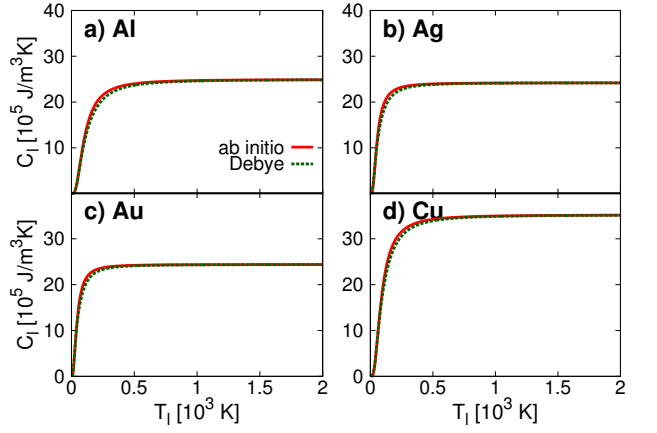


FIG. 5. Comparison of *ab initio* and Debye model predictions of the lattice heat capacity as a function of lattice temperature, $C_l(T_l)$, for (a) Al, (b) Ag, (c) Au and (d) Cu. Despite large differences in the density of states (Figure 4), the predicted lattice heat capacities of the two models agree within 10%.

is adequate for predicting the lattice heat capacity, in contrast to the remaining quantities we consider below which are highly sensitive to details of the phonons and their coupling to the electrons.

D. Electron-phonon coupling

In Section IIC we have shown that the electronic heat capacity, which determines the initial temperature that the hot electrons equilibrate to, is sensitive to electronic structure especially in noble metals at high T_e where d -bands contribute. Now we analyze the electron-phonon coupling which determines the subsequent thermalization of the hot electrons with the lattice. We show that details in the *ab initio* electron-phonon matrix elements also play a significant role, in addition to the electronic band structure, and compare previous semi-empirical estimates of the T_e -dependent phonon coupling to our direct *ab initio* calculations.

The rate of energy transfer from electrons at temperature T_e to the lattice (phonons) at temperature T_l per unit volume is given by Fermi's golden rule as

$$\begin{aligned} \frac{dE}{dt} &\equiv G(T_e)(T_e - T_l) \\ &= \frac{2\pi}{\hbar} \int_{\text{BZ}} \frac{\Omega d\mathbf{k} d\mathbf{k}'}{(2\pi)^6} \sum_{nn'\alpha} \delta(b - \hbar\omega_{\mathbf{k}'-\mathbf{k},\alpha}) \\ &\quad \times \hbar\omega_{\mathbf{k}'-\mathbf{k},\alpha} \left| g_{\mathbf{k}'n',\mathbf{k}n}^{\mathbf{k}'-\mathbf{k},\alpha} \right|^2 S_{T_e,T_l}(\varepsilon_{\mathbf{k}n}, \varepsilon_{\mathbf{k}'n'}, \hbar\omega_{\mathbf{k}'-\mathbf{k},\alpha}) \end{aligned} \quad (6)$$

with

$$\begin{aligned} S_{T_e,T_l}(\varepsilon, \varepsilon', \hbar\omega_{\text{ph}}) &\equiv f(\varepsilon, T_e) n(\hbar\omega_{\text{ph}}, T_l) (1 - f(\varepsilon', T_e)) \\ &\quad - (1 - f(\varepsilon, T_e)) (1 + n(\hbar\omega_{\text{ph}}, T_l)) f(\varepsilon', T_e). \end{aligned} \quad (7)$$

Here, Ω is the unit cell volume, $\hbar\omega_{\mathbf{q}\alpha}$ is the energy of a phonon with wave-vector $\mathbf{q} = \mathbf{k}' - \mathbf{k}$ and polarization in-

dex α , and $g_{\mathbf{k}'n',\mathbf{k}n}^{\mathbf{k}'-\mathbf{k},\alpha}$ is the electron-phonon matrix element coupling this phonon to electronic states indexed by $\mathbf{k}n$ and $\mathbf{k}'n'$.

Above, S is the difference between the product of occupation factors for the forward and reverse directions of the electron-phonon scattering process $\mathbf{k}n + \mathbf{q}\alpha \rightarrow \mathbf{k}'n'$, with $f(\varepsilon, T_e)$ and $n(\hbar\omega, T_l)$ being the Fermi and Bose distribution function for the electrons and phonons respectively. Using the fact that $S_{T_e, T_e} = 0$ for an energy-conserving process $\varepsilon + \hbar\omega_{\text{ph}} = \varepsilon'$ by detailed balance, we can write the electron-phonon coupling coefficient as

$$G(T_e) = \frac{2\pi}{\hbar} \int_{\text{BZ}} \frac{\Omega d\mathbf{k} d\mathbf{k}'}{(2\pi)^6} \sum_{nn'\alpha} \delta(\varepsilon_{\mathbf{k}'n'} - \varepsilon_{\mathbf{k}n} - \hbar\omega_{\mathbf{k}'-\mathbf{k},\alpha}) \times \hbar\omega_{\mathbf{k}'-\mathbf{k},\alpha} \left| g_{\mathbf{k}'n',\mathbf{k}n}^{\mathbf{k}'-\mathbf{k},\alpha} \right|^2 (f(\varepsilon_{\mathbf{k}n}, T_e) - f(\varepsilon_{\mathbf{k}'n'}, T_e)) \times \frac{n(\hbar\omega_{\mathbf{k}'-\mathbf{k},\alpha}, T_e) - n(\hbar\omega_{\mathbf{k}'-\mathbf{k},\alpha}, T_l)}{T_e - T_l} \quad (8)$$

This general form for *ab initio* electronic and phononic states is analogous to previous single-band / free electron theories of the electron-phonon coupling coefficient, see for example the derivation by Allen et al.³⁵

The direct *ab initio* evaluation of $G(T_e)$ using (8) requires a six-dimensional integral over electron-phonon matrix elements from DFT with very fine k -point grids that can resolve both electronic and phononic energy scales. This is impractical without the recently-developed Wannier interpolation and Monte Carlo sampling methods for these matrix elements,^{26,36} and therefore our results are the first fully *ab initio* predictions of $G(T_e)$.

Previous theoretical estimates of $G(T_e)$ are semi-empirical, combining DFT electronic structure with empirical models for the phonon coupling. For example, Wang et al.³⁷ assume that the electron-phonon matrix elements averaged over scattering angles is independent of energy and that the phonon energies are smaller than $k_B T_e$, and then approximate the electron-phonon coupling coefficient as

$$G(T_e) \approx \frac{\pi k_B}{\hbar g(\varepsilon_F)} \lambda \langle (\hbar\omega)^2 \rangle \int_{-\infty}^{\infty} d\varepsilon g^2(\varepsilon) \frac{-\partial f(\varepsilon, T_e)}{\partial \varepsilon}, \quad (9)$$

where λ is the electron-phonon mass enhancement parameter and $\langle (\hbar\omega)^2 \rangle$ is the second moment of the phonon spectrum.^{8,19,38} Lin et al.¹⁹ treat $\lambda \langle (\hbar\omega)^2 \rangle$ as an empirical parameter calibrated to experimental $G(T_e)$ at low T_e obtained from thermoreflectance measurements, and extrapolate it to higher T_e using (9). See Refs. 37 and 19 for more details.

For clarity, we motivate here a simpler derivation of an expression of the form of (9) from the general form (8). First, making the approximation $\hbar\omega_{\mathbf{q}\alpha} \ll T_e$ (which is reasonably valid for T_e above room temperature) allows us to approximate the difference between the electron occupation factors in the second line of (8) by $\hbar\omega_{\mathbf{q}\alpha} \partial f / \partial \varepsilon$ (using energy conservation). Additionally, for $T_e \gg T_l$, the third line of (8) simplifies to $k_B / (\hbar\omega_{\mathbf{k}'-\mathbf{k},\alpha})$. With no other approximations, we can then rearrange (8) to

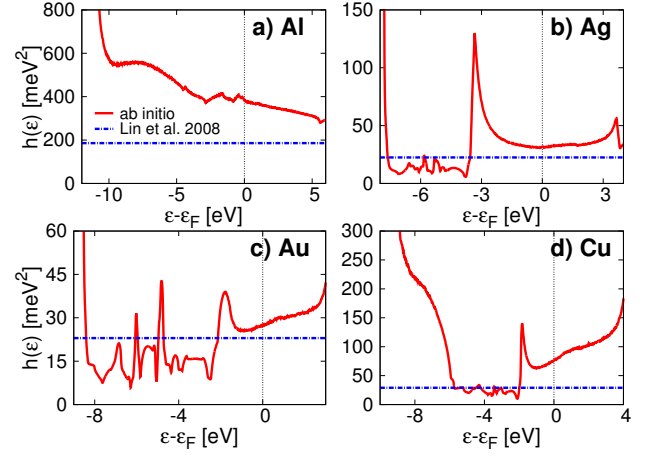


FIG. 6. Energy-resolved electron-phonon coupling strength $h(\varepsilon)$, defined by (11), for (a) Al, (b) Ag, (c) Au, (d) Cu. For the noble metals, $h(\varepsilon_F)$ is substantially larger than its value in the d -bands, which causes previous semi-empirical estimates¹⁹ using a constant $h(\varepsilon)$ to overestimate the electron-phonon coupling ($G(T_e)$) at $T_e \gtrsim 3000$ K, as shown in Fig. 7.

collect contributions by initial electron energy,

$$G(T_e) \approx \frac{\pi k_B}{\hbar g(\varepsilon_F)} \int_{-\infty}^{\infty} d\varepsilon h(\varepsilon) g^2(\varepsilon) \frac{-\partial f(\varepsilon, T_e)}{\partial \varepsilon} \quad (10)$$

with

$$h(\varepsilon) \equiv \frac{2g(\varepsilon_F)}{g^2(\varepsilon)} \int_{\text{BZ}} \frac{\Omega d\mathbf{k} d\mathbf{k}'}{(2\pi)^6} \sum_{nn'\alpha} \delta(\varepsilon - \varepsilon_{\mathbf{k}n}) \times \delta(\varepsilon_{\mathbf{k}'n'} - \varepsilon_{\mathbf{k}n} - \hbar\omega_{\mathbf{k}'-\mathbf{k},\alpha}) \hbar\omega_{\mathbf{k}'-\mathbf{k},\alpha} \left| g_{\mathbf{k}'n',\mathbf{k}n}^{\mathbf{k}'-\mathbf{k},\alpha} \right|^2. \quad (11)$$

Therefore, the primary approximation in previous semi-empirical estimates^{19,37} is the replacement of $h(\varepsilon)$ by an energy-independent constant $\lambda \langle (\hbar\omega)^2 \rangle$, used as an empirical parameter.

Fig. 6 compares *ab initio* calculations of this energy-resolved electron-phonon coupling strength, $h(\varepsilon)$, with previous empirical estimates of $\lambda \langle (\hbar\omega)^2 \rangle$, and Fig. 7 compares the resulting temperature dependence of the electron-phonon coupling, $G(T_e)$, from the *ab initio* (8) and semi-empirical methods (9). For noble metals, $G(T_e)$ increases sharply beyond $T_e \sim 3000$ K because of the large density of states in the d -bands. However, $h(\varepsilon)$ is smaller by a factor of 2 – 3 in the d -bands compared to near the Fermi level. Therefore, assuming $h(\varepsilon)$ to be an empirical constant^{17,19} results in a significant overestimate of $G(T_e)$ at high T_e , compared to the direct *ab initio* calculations. Additionally, the shallowness of the d -bands in the semi-local PBE band structure used in Ref. 19 lowers the onset temperature of the increase in $G(T_e)$, and results in further overestimation compared to our *ab initio* predictions.

The *ab initio* predictions agree very well with the experimental measurements of $G(T_e)$ available at lower temperatures for noble metals.^{3,14,15,39,40} In fact, the semi-empirical calculation based on $\lambda \langle (\hbar\omega)^2 \rangle$ underestimates

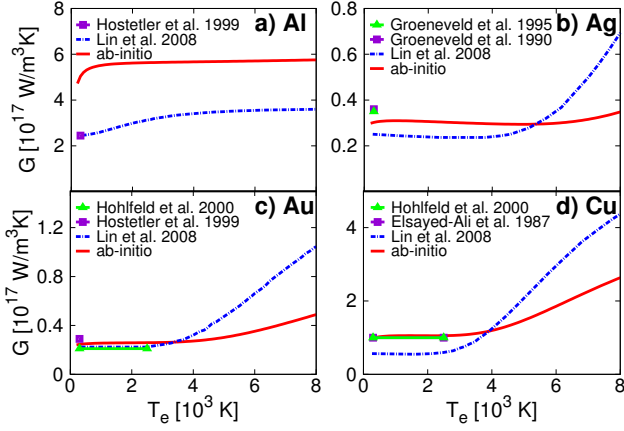


FIG. 7. Comparison of predictions of the electron-phonon coupling strength as a function of electron temperature, $G(T_e)$, for (a) Al, (b) Ag, (c) Au and (d) Cu, with experimental measurements where available.^{3,14,15,39,40} The DFT-based semi-empirical predictions of Lin et al.¹⁹ overestimate the coupling for noble metals at high temperatures because they assume an energy-independent electron-phonon coupling strength (Figure 6) and neglect the weaker phonon coupling of d -bands compared to the conduction band. The experimental results (and hence the semi-empirical predictions) for aluminum underestimate electron-phonon coupling because they include the effect of competing electron-electron thermalization which happens on the same time scale.

the room temperature electron-phonon coupling for these metals; the significant overestimation of $G(T_e)$ seen in Fig. 7 is in spite of this partial cancellation of error. This shows the importance of *ab initio* electron-phonon matrix elements in calculating the coupling between hot electrons and the lattice.

Experimental measurements of the electron-phonon coupling in noble metals are reliable because of the reasonably clear separation between a fast electron-electron thermalization rise followed by a slower electron-phonon decay in the thermoreflectance signal. In aluminum, these time scales significantly overlap making an unambiguous experimental determination of G difficult. Consequently, the value of G for Al is not well agreed upon.⁴¹ For example, in Ref. 39, there is no fast transient free-electron

spike and G is extracted from the lattice temperature variation instead. However, the measured rate for the lattice temperature rise includes competing contributions from electron-electron and electron-phonon thermalization; attributing the entire rate to electron-phonon coupling only provides a lower bound for G . Indeed, figure 7(a) shows that this experimental estimate³⁹ and its phenomenological extension to higher T_e ¹⁹ significantly underestimate our *ab initio* predictions by almost a factor of two. Note that density-functional theory is highly reliable for the mostly free-electron-like band structure of aluminum, and the *ab initio* electron-phonon matrix elements are accurate to within 5 %.²⁶ We therefore conclude that electron-electron thermalization is only about two times faster than electron-phonon thermalization in aluminum, causing the significant discrepancy in experimental measurements. This further underscores the importance of *ab initio* calculations over phenomenological models of electron-phonon coupling.

E. Dielectric Function

The final ingredient for a complete *ab initio* description of ultrafast transient absorption measurements is the temperature-dependent dielectric function of the material. We previously showed²⁶ that we could predict the imaginary part of the dielectric function $\text{Im } \epsilon(\omega)$ of plasmonic metals in quantitative agreement with ellipsometric measurements for a wide range of frequencies by accounting for the three dominant contributions,

$$\text{Im } \epsilon(\omega) = \frac{4\pi\sigma_0}{\omega(1 + \omega^2\tau^2)} + \text{Im } \epsilon_{\text{direct}}(\omega) + \text{Im } \epsilon_{\text{phonon}}(\omega). \quad (12)$$

We briefly summarize the calculation of these contributions and focus on their electron temperature dependence below; see Ref. 26 for a detailed description.

The first term of (12) accounts for the Drude response of the metal due to free carriers near the Fermi level, with the zero-frequency conductivity σ_0 and momentum relaxation time τ calculated using the linearized Boltzmann equation with *ab initio* collision integrals. The second and third terms of (12),

$$\text{Im } \epsilon_{\text{direct}}(\omega) = \frac{4\pi^2 e^2}{m_e^2 \omega^2} \int_{\text{BZ}} \frac{d\mathbf{k}}{(2\pi)^3} \sum_{n'n} (f_{\mathbf{k}n} - f_{\mathbf{k}n'}) \delta(\varepsilon_{\mathbf{k}n'} - \varepsilon_{\mathbf{k}n} - \hbar\omega) \left| \hat{\lambda} \cdot \langle \mathbf{p} \rangle_{n'n}^{\mathbf{k}} \right|^2, \quad \text{and} \quad (13)$$

$$\begin{aligned} \text{Im } \epsilon_{\text{phonon}}(\omega) = & \frac{4\pi^2 e^2}{m_e^2 \omega^2} \int_{\text{BZ}} \frac{d\mathbf{k}' d\mathbf{k}}{(2\pi)^6} \sum_{n'n\alpha\pm} (f_{\mathbf{k}n} - f_{\mathbf{k}'n'}) \left(n_{\mathbf{k}'-\mathbf{k},\alpha} + \frac{1}{2} \mp \frac{1}{2} \right) \delta(\varepsilon_{\mathbf{k}'n'} - \varepsilon_{\mathbf{k}n} - \hbar\omega \mp \hbar\omega_{\mathbf{k}'-\mathbf{k},\alpha}) \\ & \times \left| \hat{\lambda} \cdot \sum_{n_1} \left(\frac{g_{\mathbf{k}'n',\mathbf{k}n_1}^{\mathbf{k}'-\mathbf{k},\alpha} \langle \mathbf{p} \rangle_{n_1 n}^{\mathbf{k}}}{\varepsilon_{\mathbf{k}n_1} - \varepsilon_{\mathbf{k}n} - \hbar\omega + i\eta} + \frac{\langle \mathbf{p} \rangle_{n'n_1}^{\mathbf{k}'} g_{\mathbf{k}'n_1,\mathbf{k}n}^{\mathbf{k}'-\mathbf{k},\alpha}}{\varepsilon_{\mathbf{k}'n_1} - \varepsilon_{\mathbf{k}n} \mp \hbar\omega_{\mathbf{k}'-\mathbf{k},\alpha} + i\eta} \right) \right|^2, \quad (14) \end{aligned}$$

capture the contributions due to direct interband excita-

tions and phonon-assisted intraband excitations respec-

tively. Here $\langle \mathbf{p} \rangle_{n'n}^{\mathbf{k}}$ are matrix elements of the momentum operator, $\hat{\lambda}$ is the electric field direction (results are isotropic for crystals with cubic symmetry), and all remaining electron and phonon properties are exactly as described previously. The energy-conserving δ -functions are replaced by a Lorentzian of width equal to the sum of initial and final electron linewidths, because of the finite lifetime of the quasiparticles.

The dielectric function calculated using (12-14) depends on the electron temperature T_e in two ways. First, the electron occupations $f_{\mathbf{k}n}$ directly depend on T_e . Second, the phase-space for electron-electron scattering increases with electron temperature, which increases the momentum relaxation rate (τ^{-1}) in the first Drude term of (12) and the Lorentzian broadening in the energy conserving δ -function in (13) and (14).

We calculate *ab initio* electron linewidths using Fermi golden rule calculations for electron-electron and electron-phonon scattering at room temperature, as detailed in Ref. 26. These calculations are computationally expensive and difficult to repeat for several electron temperatures; we use the *ab initio* linewidths at room temperature with an analytical correction for the T_e dependence. The electron-phonon scattering rate depends on the lattice temperature, but is approximately independent of T_e because the phase space for scattering is determined primarily by the electronic density-of-states and electron-phonon matrix elements, which depend strongly on the electron energies but not on the occupation factors or T_e . The phase space for electron-electron scattering, on the other hand, depends on the occupation factors and T_e because an electron at an energy far from the Fermi level can scatter with electrons close to the Fermi level. The variation of this phase-space with temperature is primarily due to the change in occupation of states near the Fermi level, and we can therefore estimate this effect in plasmonic metals using a free electron model.

Within a free electron model, the phase-space for electron-electron scattering grows quadratically with energy relative to the Fermi level, resulting in scattering rates $\propto (\varepsilon - \varepsilon_F)^2$ at zero electron temperatures, as is well-known.^{2,42} We can extend these derivations to finite electron temperature to show that the energy and temperature-dependent electron-electron scattering rate

$$\tau_{ee}^{-1}(\varepsilon, T_e) \approx \frac{D_e}{\hbar} [(\varepsilon - \varepsilon_F)^2 + (\pi k_B T_e)^2] \quad (15)$$

for $|\varepsilon - \varepsilon_F| \ll \varepsilon_F$ and $T_e \ll \varepsilon_F/k_B$. Within the free electron model, the constant of proportionality $D_e = \frac{m_e e^4}{4\pi \hbar^2 (\epsilon_b^0)^2 \epsilon_S^{3/2} \sqrt{\varepsilon_F}} \left(\frac{\sqrt{4\varepsilon_F \varepsilon_S}}{4\varepsilon_F + \varepsilon_S} + \tan^{-1} \sqrt{\frac{4\varepsilon_F}{\varepsilon_S}} \right)$, where the background dielectric constant ϵ_b^0 and the Thomas-Fermi screening energy scale ε_S are typically treated as empirical parameters.² Here, we extract D_e by fitting (15) to the *ab initio* electron-electron scattering rates at room temperature T_0 .²⁶ The resulting fit parameters are shown in Table I. We then estimate the total scattering rates at other temperatures by adding $(D_e/\hbar)(\pi k_B)^2(T_e^2 - T_0^2)$ to the total *ab initio* results (including electron-phonon scattering) at T_0 .

TABLE I. Parameters to describe the change in dielectric function with electron temperature using (16), extracted from fits to *ab initio* calculations. The energies and effective masses for the parabolic band approximation for the $d \rightarrow s$ transition in noble metals are indicated Figure 12(a).

	Al	Ag	Au	Cu
Physical constants:				
ω_p [eV/ \hbar]	15.8	8.98	9.01	10.8
τ^{-1} [eV/ \hbar]	0.0911	0.0175	0.0240	0.0268
Fits to <i>ab initio</i> calculations:				
D_e [eV ⁻¹]	0.017	0.021	0.016	0.020
A_0 [eV ^{3/2}]	-	70	22	90
ε_c [eV]	-	0.31	0.96	0.98
ε_0 [eV]	-	3.36	1.25	1.05
m_v^*/m_c^*	-	5.4	3.4	16.1

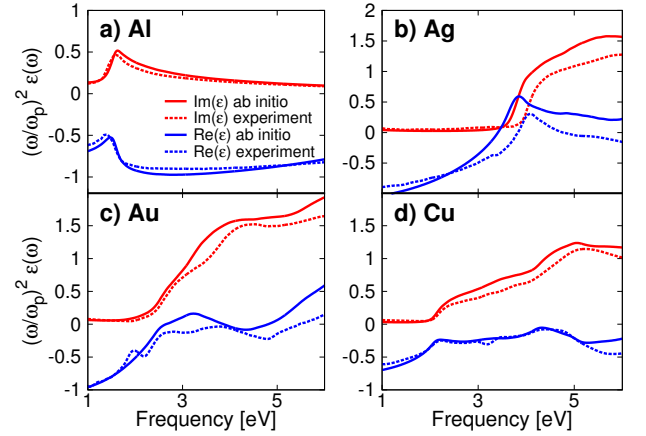


FIG. 8. Predicted complex dielectric functions for (a) Al, (b) Ag, (c) Au, (d) Cu at room temperature (300 K) compared with ellipsometry measurements.⁴³ The y -axis is scaled by ω^2/ω_p^2 in order to represent features at different frequencies such as the Drude pole and the interband response on the same scale.

Finally, we use the Kramers-Kronig relations to calculate $\text{Re}(\epsilon(\omega, T_e))$ from $\text{Im}(\epsilon(\omega, T_e))$. Figure 8 compares the predicted dielectric functions with ellipsometry measurements⁴³ for a range of frequencies spanning from near-infrared to ultraviolet. Note that we scale the y -axis by $(\omega/\omega_p)^2$, where $\omega_p = \sqrt{4\pi e^2 n_e/m_e}$ is the free-electron plasma frequency, in order to display features at all frequencies on the same scale. We find excellent agreement for aluminum within 10 % of experiment over the entire frequency range, including the peak around 1.6 eV due to an interband transition. The agreement is reasonable for noble metals with a typical error within 20 %, but with a larger error ~ 50 % for certain features in the interband $d \rightarrow s$ transitions due to inaccuracies in the d -band positions predicted by DFT (especially for silver).

Figures 9, 10 and 11 show the change of the complex dielectric function upon increasing the electron temperature T_e from room temperature to 400 K, 1000 K and 5000 K respectively, while the lattice remains at

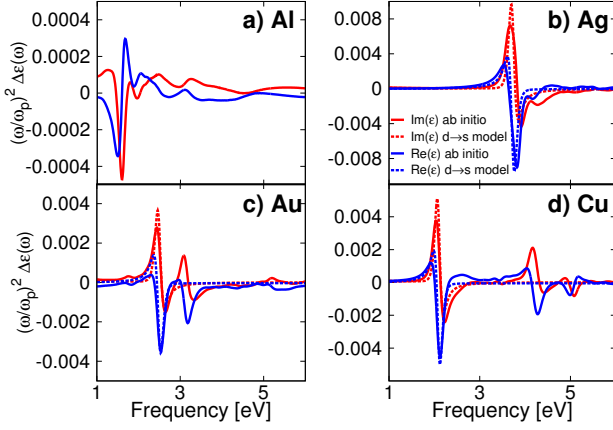


FIG. 9. Change in the predicted complex dielectric function for (a) Al, (b) Ag, (c) Au, (d) Cu from room temperature (300 K) to electron temperature $T_e = 400$ K (with the lattice remaining at room temperature). The analytical model given by (16), with fit parameters summarized in Table I captures the essential features of the *ab initio* data for noble metals at lower temperatures, but misses the contributions of broadening due to electron-electron scattering at higher temperatures. Note that the y -axis is scaled as in Fig. 8 for clarity.

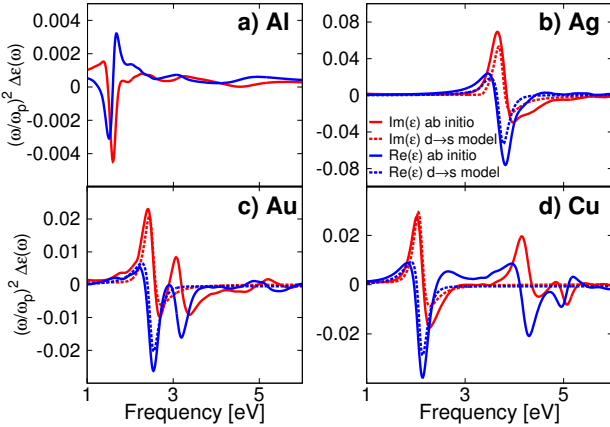


FIG. 10. Change in the predicted complex dielectric function for (a) Al, (b) Ag, (c) Au, (d) Cu from room temperature (300 K) to electron temperature $T_e = 1000$ K (with the lattice remaining at room temperature).

room temperature.⁴⁴ For all four metals, the response from infrared to ultraviolet frequencies is dominated by ‘sharp’ features due to interband transitions that broaden with increasing temperature, rather than a change in the Drude response which would be the only contribution in a free-electron model.

The strongest temperature dependence in noble metals results from transitions between the highest occupied d -band to the Fermi level near the L point, as shown in Figure 12(a). Assuming a parabolic dispersion and a constant transition matrix element, and accounting for the change in the Drude response, this temperature depen-

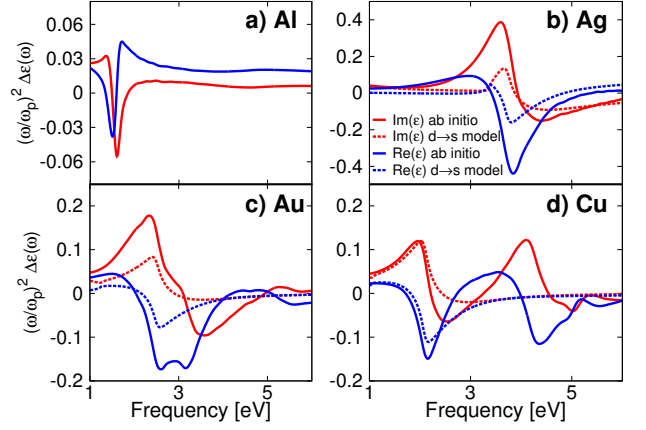


FIG. 11. Change in the predicted complex dielectric function for (a) Al, (b) Ag, (c) Au, (d) Cu from room temperature (300 K) to electron temperature $T_e = 5000$ K (with the lattice remaining at room temperature).

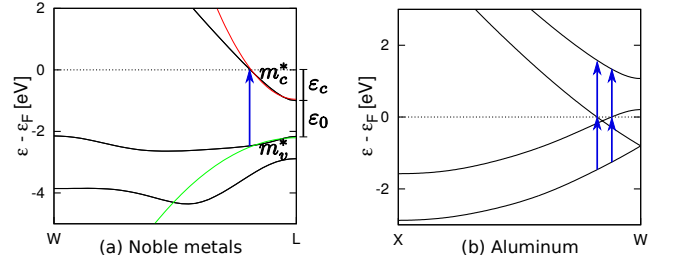


FIG. 12. Critical interband transitions determining the ‘sharp’ features in the dielectric function change for (a) noble metals (gold shown; similar shapes for silver and copper) and (b) aluminum. A parabolic band model around the L point (parameters in Table I) approximates the critical transition in noble metals. This is difficult in aluminum because of four such transitions in a narrow energy range $\approx 1.3 - 1.6$ eV.

dence can be modeled as^{17,45}

$$\Delta\epsilon(\omega) = -\Delta \left[\frac{\omega_p^2}{\omega(\omega + i(\tau^{-1} + \frac{D_e}{\hbar}(\pi k_B T_e)^2))} + \mathcal{K} \frac{A_0}{(\hbar\omega)^2} \int_{-\epsilon_c}^{\infty} \frac{d\epsilon(1 - f(\epsilon, T_e))}{\sqrt{\frac{m_v^*}{m_c^*}(\hbar\omega - (\epsilon + \epsilon_0 + \epsilon_c)) - (\epsilon + \epsilon_c)}} \right]. \quad (16)$$

The denominator in the second term captures the joint density of states for transitions between the bands, and the numerator counts unoccupied states near the Fermi level, which introduces the temperature dependence. Above, \mathcal{K} fills in the real part of the dielectric function, given the imaginary part using the Kramers-Kronig relation.

Table I lists the parameters for the parabolic band approximation obtained from the *ab initio* band structures. Figure 9 shows that this approximation captures the correct shape of $\Delta\epsilon(\omega)$ for small changes in T_e . However, this model underestimates the T_e dependence for higher

T_e because it ignores the quadratic increase in broadening of the electronic states due to increased electron-electron scattering, as Figures 10 and 11 show. Aluminum exhibits a sharp change in the dielectric function around $\hbar\omega \approx 1.5$ eV, which results from several transitions to/from the Fermi level near the W point as Figure 12(b) shows. Additionally two of the involved bands are not parabolic, making it difficult to construct a simple model like (16). Therefore, simplified models are adequate for qualitative analysis of lower temperature excitation experiments in noble metals,¹⁷ but *ab initio* dielectric functions are necessary for a quantitative analysis of higher temperature experiments and a wider range of materials and probe frequencies.

CONCLUSIONS

Ab initio calculations of electron-phonon coupling, electron and lattice heat capacities, and dielectric functions show qualitative differences from free-electron and previous semi-empirical estimates because of the substantial energy dependence of electron-phonon matrix elements and electronic density of states. These changes are particularly important for gold and copper at transient electron temperatures greater than 2000 K because of the change in occupations of the *d*-bands situated ~ 2 eV below the Fermi level in these metals.

The temperature dependence of the optical response is, in particular, important for a wide range of applications beyond understanding ultrafast measurements. We show that while simple models can account for some of the qualitative features of the change in dielectric function for small changes in temperature, *ab initio* treatment is essential to quantitatively account for the complete

frequency and temperature dependence, including effects such as carrier linewidth broadening and transitions between multiple non-parabolic bands. Given the dearth of published temperature-dependent dielectric functions in the literature, we include detailed tables of our *ab initio* predictions for electron temperatures up to 8000 K, and spanning frequencies from the infrared to the ultraviolet, in the supplementary information.⁴⁴

This work has direct implications for analysis of experimental pump-probe studies of metal nanostructures and is the subject of ongoing work in our group. With the predicted material properties we anticipate a parameter-free description of the spectra obtained in transient absorption studies since we implicitly account for all the microscopic processes in the non-equilibrium dynamics of electrons in plasmonic metals.

ACKNOWLEDGEMENTS

This material is based upon work performed by the Joint Center for Artificial Photosynthesis, a DOE Energy Innovation Hub, supported through the Office of Science of the U.S. Department of Energy under Award Number DE-SC0004993. This research used resources of the National Energy Research Scientific Computing Center, a DOE Office of Science User Facility supported by the Office of Science of the U.S. Department of Energy under Contract No. DE-AC02-05CH11231. P. N. is supported by a National Science Foundation Graduate Research Fellowship and by the Resnick Sustainability Institute. A. B. is supported by a National Science Foundation Graduate Research Fellowship, a Link Foundation Energy Fellowship, and the DOE ‘Light-Material Interactions in Energy Conversion’ Energy Frontier Research Center (DE-SC0001293).

-
- ¹ S. I. Anisimov, B. L. Kapeliovich, and T. L. Perelman, Zh. Eksp. Teor. Fiz **66**, 375 (1974).
 - ² N. Del Fatti, C. Voisin, M. Achermann, S. Tzortzakis, D. Christofilos, and F. Vallée, Phys. Rev. B **61**, 16956 (2000).
 - ³ H. Elsayed-Ali, T. Norris, M. Pessot, and G. Mourou, Phys. Rev. Lett. **58**, 1212 (1987).
 - ⁴ H. E. Elsayed-Ali, T. Juhasz, G. O. Smith, and W. E. Bron, Phys. Rev. B **43**, 4488 (1991).
 - ⁵ A. Giri, J. T. Gaskins, B. M. Foley, R. Cheaito, and P. E. Hopkins, Journal of Applied Physics, 044305 (2015).
 - ⁶ G. V. Hartland, Chemical Reviews **111**, 3858 (2011).
 - ⁷ M. I. Kaganov, I. M. Lifshitz, and L. V. Tanatarov, Soviet Physics JETP-USSR **4**, 173 (1957).
 - ⁸ G. Grimvall, *The electron-phonon interaction in metals*, Vol. 8 (North-Holland Amsterdam, 1981).
 - ⁹ Y. Gan, C. Wang, and Z. Chen, Opt. Lett. **40**, 340 (2015).
 - ¹⁰ S. Link and E.-S. M. A., The Journal of Physical Chemistry B **103**, 8410 (1999).
 - ¹¹ T. Luo and G. Chen, Phys. Chem. Chem. Phys. **15**, 3389 (2013).
 - ¹² P. M. Norris, A. P. Caffrey, R. J. Stevens, J. M. Klopff, J. T. McLeskey, and A. N. Smith, Review of Scientific Instruments **74**, 400 (2003).
 - ¹³ B. Y. Mueller and B. Rethfeld, *E-MRS 2013 Symposium V: “Laser Material Interactions for Micro- and Nano-Applications” 27–31 May 2013, Strasbourg (France)*, Applied Surface Science **302**, 24 (2014).
 - ¹⁴ R. H. Groeneveld, R. Sprik, and A. Lagendijk, Phys. Rev. Lett. **64**, 784 (1990).
 - ¹⁵ R. H. Groeneveld, R. Sprik, and A. Lagendijk, Phys. Rev. B **51**, 11433 (1995).
 - ¹⁶ B. Rethfeld, A. Kaiser, M. Vicanek, and G. Simon, Phys. Rev. B **65**, 214303 (2002).
 - ¹⁷ C.-K. Sun, F. Vallée, L. H. Acioli, E. P. Ippen, and J. G. Fujimoto, Phys. Rev. B **50**, 15337 (1994).
 - ¹⁸ Y. Ma, Journal of Applied Physics **116**, 243505 (2014).
 - ¹⁹ Z. Lin and L. V. Zhigilei, Phys. Rev. B, 075133 (2008).
 - ²⁰ L. D. Landau and E. M. Lifschitz, *Electrodynamics of Continuous Media, Course of Theoretical Physics*, Vol. 8 (Pergamon Press, Oxford, 1960).
 - ²¹ J. M. Ziman, *Electrons and Phonons* (Clarendon Press, Oxford, 1962).

- ²² N. W. Ashcroft and N. D. Mermin, *Solid State Physics* (Holt, Rinehart and Winston: New York, 1976).
- ²³ D. Pines and P. Nozieres, *Normal Fermi Liquids, The Theory of Quantum Liquids*, Vol. 1 (Addison-Wesley, New York, 1966).
- ²⁴ S. Link, C. Burda, M. B. Mohamed, B. Nikoobakht, and M. A. El-Sayed, *The Journal of Physical Chemistry A*, **J. Phys. Chem. A** **103**, 1165 (1999).
- ²⁵ D. Lide, *CRC Handbook of Chemistry and Physics, 84th Edition*, CRC HANDBOOK OF CHEMISTRY AND PHYSICS (Taylor & Francis, 2003).
- ²⁶ A. Brown, R. Sundararaman, P. Narang, W. A. Goddard III, and H. A. Atwater, *ACS Nano* **10**, 957 (2016).
- ²⁷ R. Sundararaman, D. Gunceler, K. Letchworth-Weaver, and T. A. Arias, “JDFTx,” <http://jdftx.sourceforge.net> (2012).
- ²⁸ J. P. Perdew, A. Ruzsinszky, G. I. Csonka, O. A. Vydrov, G. E. Scuseria, L. A. Constantin, X. Zhou, and K. Burke, *Phys. Rev. Lett.* **100**, 136406 (2008).
- ²⁹ S. L. Dudarev, G. A. Botton, S. Y. Savrasov, C. J. Humphreys, and A. P. Sutton, *Phys. Rev. B* **57**, 1505 (1998).
- ³⁰ R. Sundararaman, P. Narang, A. S. Jermyn, W. A. Goddard III, and H. A. Atwater, *Nat. Commun.* **5**, 12 (2014).
- ³¹ I. Souza, N. Marzari, and D. Vanderbilt, *Phys. Rev. B* **65**, 035109 (2001).
- ³² J. P. Perdew, K. Burke, and M. Ernzerhof, *Phys. Rev. Lett.* **77**, 3865 (1996).
- ³³ C. Voisin, N. Del Fatti, D. Christofilos, and F. Vallée, *The Journal of Physical Chemistry B* **105**, 2264 (2001).
- ³⁴ J. H. Hodak, A. Henglein, and G. V. Hartland, *The Journal of Physical Chemistry B* **104**, 9954 (2000).
- ³⁵ P. B. Allen, *Phys. Rev. Lett.* **59**, 1460 (1987).
- ³⁶ F. Giustino, M. L. Cohen, and S. G. Louie, *Phys. Rev. B* **76**, 165108 (2007).
- ³⁷ X. Y. Wang, D. M. Riffe, Y.-S. Lee, and M. C. Downer, *Phys. Rev. B* **50**, 8016 (1994).
- ³⁸ W. McMillan, *Phys. Rev.* **167**, 331 (1968).
- ³⁹ J. L. Hostetler, A. N. Smith, D. M. Czajkowsky, and P. M. Norris, *Applied Optics* **38**, 3614 (1999).
- ⁴⁰ J. Hohlfeld, S.-S. Wellershoff, J. Güdde, U. Conrad, V. Jähnke, and E. Matthias, *Chemical Physics* **251**, 237 (2000).
- ⁴¹ C. Guo, G. Rodriguez, A. Lobad, and A. Taylor, *Phys. Rev. Lett.* **84**, 4493 (2000).
- ⁴² F. Ladstädter, U. Hohenester, P. Puschnig, and C. Ambrosch-Draxl, *Phys. Rev. B* **70**, 235125 (2004).
- ⁴³ E. D. Palik, *Handbook of Optical Constants of Solids* (Academic, New York, 1985).
- ⁴⁴ See supplementary information for plots of the complex dielectric function at several electron temperatures, and complete datasets as a function of temperature and frequency for use in numerical analyses.
- ⁴⁵ R. Rosei, F. Antonangeli, and U. Grassano, *Surface Science* **37**, 689 (1973).